Excitation of terahertz surface plasmons on graphene surfaces by an elementary dipole and quantum emitter: Strong electrodynamic effect of dielectric support

George W. Hanson,[1,*] Ebrahim Forati,[1,†] Whitney Linz,[1,‡] and Alexander B. Yakovlev[2,§]

[1]*Department of Electrical Engineering, University of Wisconsin-Milwaukee, 3200 N. Cramer St., Milwaukee, Wisconsin 53211, USA*

[2]*Center for Applied Electromagnetic Systems Research (CAESR), Department of Electrical Engineering, The University of Mississippi, University, MS 38677, USA*

(Received 11 September 2012; published 26 December 2012)

The excitation of transverse magnetic (TM) surface plasmons by a point dipole in the vicinity of a multilayered graphene/dielectric system is examined. It was previously shown that the surface plasmon (SP) excited by a vertical dipole on an isolated graphene sheet exhibits a strong excitation peak in the THz region; here we show that, in the presence of a finite-thickness dielectric support layer such as SiO_2, considerable spectral content is transferred to a second (perturbed dielectric slab) mode, greatly decreasing and redshifting the excitation peak. The presence of a Si half-space also diminishes the excitation strength, but for graphene on top of SiO_2-Si the presence of the SiO_2 layer creates a spacer restoring the excitation peak. A two-level quantum emitter is also considered, where it is shown that the addition of a thin dielectric support slab and SiO_2-Si geometries affects the spontaneous decay rate in a manner similar to the classical dipole SP excitation peak.

DOI: 10.1103/PhysRevB.86.235440 PACS number(s): 78.67.Wj, 78.20.Bh, 41.20.Jb

I. INTRODUCTION

Recently, large-area graphene has been fabricated,[1,2] allowing for graphene plasmonic applications in the far- through near-infrared range of frequencies. Graphene has been proposed for applications such as THz plasmon oscillators,[3] polarizers,[4,5] filters,[6] antennas,[7,8] surface plasmon modulators,[9] and in tunable waveguiding structures and interconnects,[10–17] among a host of other applications such as Fourier optics and beam scanning[18,19] and cloaking.[20]

For plasmonic applications there are four important attributes of the surface plasmon (SP): (1) attenuation, (2) propagation constant, (3) mode confinement and field profile, and (4) excitation strength. The first three fundamental plasmon properties have been studied in previous works (e.g., Refs. 21–24), and in Ref. 25 the existence of transverse electric/magnetic graphene plasmons was examined in light of the intraband and interband contributions to the conductivity. In our previous work[26] we have examined the dipole excitation problem of a single graphene sheet at the intersection of two dielectric half-spaces (see also Refs. 27 and 28 for the quantum emitter case). In the THz regime it was shown that surface plasmons on graphene have higher attenuation, but also much better field confinement, than a thin metal layer. Furthermore, in the low THz regime it was found that the surface plasmon can be strongly excited, with the electric field being several orders of magnitude larger than the field in the absence of the graphene sheet (which is not the case for thin metal sheets). These strong surface plasmon absorption peaks at THz frequencies have been measured for several graphene structures.[29,30] Further, recent scattering-type scanning near-field optical microscopy (SNOM) imaging experiments[31] have shown in real space the existence of graphene surface plasmons on finite graphene structures, and confirmed some basic SP properties predicted by previous models, as well as some of the results obtained here.

Most of the results in Ref. 26 and many of the results in other previous theoretical/simulation studies of electrodynamic effects predominately considered the graphene sheet to reside in vacuum (i.e., suspended graphene[32,33]). Other than suspended graphene, graphene is often used in various multilayer environments, such as graphene-SiO_2-Si and supported graphene on SiO_2 or other thin layers.[34,35] In Ref. 26 it was shown that the introduction of a dielectric half-space tends to depress the excitation peak, and increase field confinement and attenuation.

In this work, we again study the four above-mentioned surface plasmon attributes based on the dipole excitation problem, and focus on the electrodynamic effect of a finite-thickness dielectric slab, and, more generally, a multilayered graphene/dielectric system on graphene-supported surface plasmons. The electromagnetic fields are governed by classical Maxwell's equations, and the graphene is represented by a conductivity surface arising from a semiclassical (intraband) and quantum-dynamical (interband) model.

It is shown that surface plasmons on supported graphene on SiO_2 are considerably different than on suspended graphene, and that even an electrically-thin dielectric support can eliminate the SP excitation peak exhibited by an isolated graphene layer, and decrease field confinement by transferring spectral content to a dielectric-slab surface mode weakly bound to the substrate. However, the graphene rapidly (in space) decouples from a dielectric support by introducing a low-permittivity gap between the graphene sheet and the dielectric, restoring the SP excitation peak. For graphene on silicon, enhanced field confinement depresses the excitation peak, but the addition of a low-permittivity spacer can restore the peak. Finally, we consider a two-level quantum emitter and examine the effect of the dielectric environment on the spontaneous decay rate,[28] where, similar to the classical excitation case, the presence of the dielectric support tends to decrease the decay rate by opening additional decay channels into dielectric slab modes. In the presence of a Si half-space, as with the classical dipole, the addition of a spacer layer enhances the decay rate. In the following all units are in the SI system, and the time variation (suppressed) is $e^{j\omega t}$, where j is the imaginary unit.

II. DESCRIPTION

Figure 1 depicts a laterally infinite graphene sheet having conductivity σ (S) above a dielectric slab having permittivity

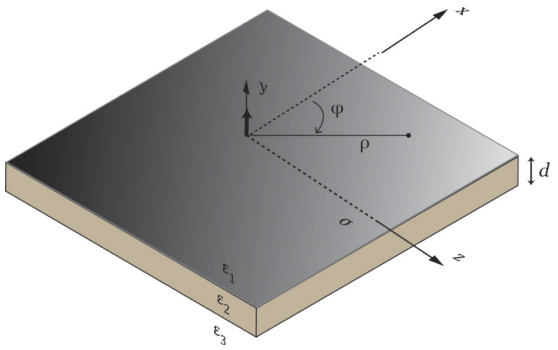

FIG. 1. (Color online) A graphene sheet characterized by surface conductivity σ above a dielectric slab having permittivity ε_2 and thickness d. A source dipole excites the structure.

ε_2. Upper and lower half-spaces are semi-infinite and have permittivities ε_1 and ε_3, respectively. The source dipole (thick arrow) is shown as being vertically aligned, but a horizontal dipole is also considered in what follows.

The graphene sheet is represented by an infinitesimally thin, local, two-sided surface characterized by a surface conductivity $\sigma(\omega,\mu_c,\gamma,T)$, where ω is radian frequency, μ_c is chemical potential, γ is a phenomenological scattering rate that is assumed to be independent of energy ε, and T is temperature. Mathematical details of the graphene model, dipole excitation, and resulting fields are provided in the Appendix. Briefly, the graphene conductivity used here results from the Kubo formula,[36] Eq. (A1), and the fields due to an infinitesimal dipole are given in terms of Sommerfeld integrals. As in Ref. 26 for the given impedance surface model of graphene the electromagnetic solution is exact.

In all cases we assume $\gamma = 1/\tau = 1.32$ meV ($\tau = 0.5$ ps, corresponding to a mean free path of several hundred nanometers), and $T = 300$ K. The value of the scattering rate is similar to that measured in Refs. 37 (1.1 ps), 38 (0.35 ps), and 39 (0.33 ps), where a Drude conductivity was verified in the far-infrared region. Furthermore, we assume nondispersive dielectrics to focus on graphene's electrodynamic response rather than on the substrate response; however, for highly dispersive dielectrics such as SiC the measured permittivity or a Lorentzian model could be used. Finally, we ignore dielectric loss, which is sufficient for SiO_2 and for silicon with low doping.

III. RESULTS

A. Single graphene layer, suspended and supported

In this section we set $\varepsilon_1 = \varepsilon_3 = 1$ to implement vacuum half-spaces. The source dipole is vertically oriented and placed on the graphene surface $y = \rho = 0$. The vertical dipole excites only TM surface plasmons and can be used to model the probe of a scanning optical microscope.[31] However, the resulting electric field has all three components $E_{x,y,z}$. As discussed in,[26] at high frequency ($k_\rho^{SP} \gg k_0$; where k_ρ^{SP} and k_0 are the surface plasmon and free-space wavenumbers, respectively) the three field components have similar magnitude, and at low frequency the vertical field component is dominant. Therefore, in the following we concentrate on the vertical field component. The electric field is normalized by the vertical component

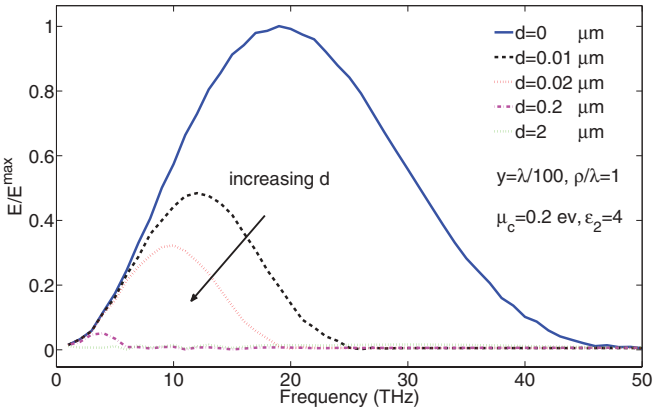

FIG. 2. (Color online) Normalized vertical electric field magnitude, Eq. (A7), at vertical position $y = \lambda/100$ and radial distance $\rho/\lambda = 1$ for a suspended graphene sheet ($d = 0$, $\mu_c = 0.2$ eV) and for supported graphene with increasing slab thickness values for an $\varepsilon_2 = 4$ dielectric slab.

of the direct (free-space) field E_y^{max}, i.e., the field that would be present in the absence of the graphene surface and dielectric regions 2 and 3; see Eq. (A11).

Figure 2 shows the normalized vertical electric field magnitude very close to the graphene sheet, at vertical position $y = \lambda/100$, and radial distance $\rho/\lambda = 1$, where λ is the vacuum wavelength. Results are shown for an isolated (suspended) graphene sheet ($d = 0$) having $\mu_c = 0.2$ eV (charge density $n \simeq 3.4 \times 10^{12}$ cm^{-2}) and for supported graphene (graphene on a finite-thickness slab) with increasing slab thickness values. The permittivity of the dielectric slab is $\varepsilon_2 = 4$, the approximate value of $Si0_2$ in the low THz region. Figure 3 shows the result when $\mu_c = 0.5$ eV (charge density $n \simeq 2 \times 10^{13}$ cm^{-2}); behavior similar to that in Fig. 2 is observed but with a larger peak occurring at higher frequencies (consistent with the measured results in Ref. 29 as bias is varied).

It can be seen from Figs. 2 and 3 that the presence of even an electrically thin dielectric support layer can significantly diminish the excitation peak of suspended graphene. In the

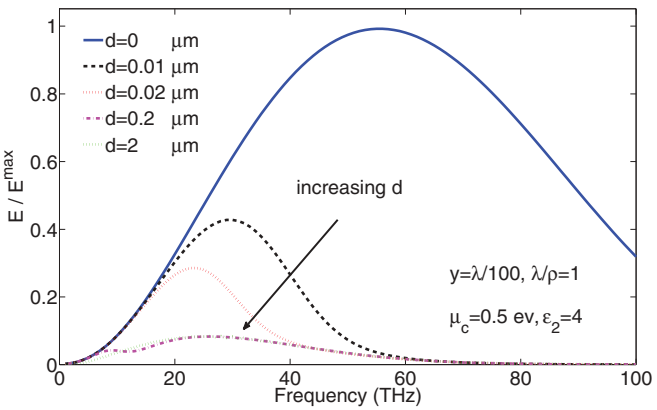

FIG. 3. (Color online) Normalized vertical electric field magnitude, Eq. (A7), at vertical position $y = \lambda/100$ and radial distance $\rho/\lambda = 1$ for a suspended graphene sheet ($d = 0$, $\mu_c = 0.5$ eV) and for supported graphene with increasing slab thickness values for an $\varepsilon_2 = 4$ dielectric slab.

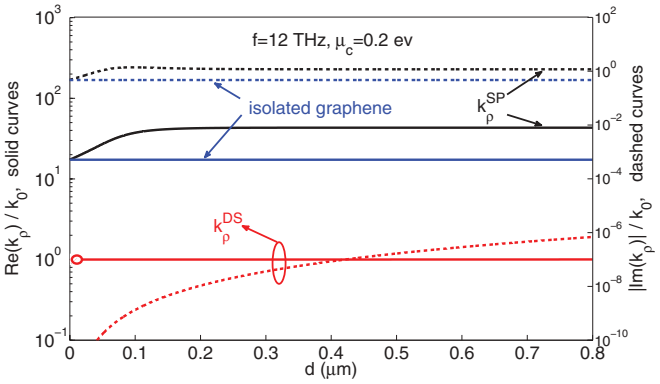

FIG. 4. (Color online) Complex propagation constant k_ρ for isolated (suspended) graphene, and for the case of supported graphene as dielectric thickness d varies ($\varepsilon_2 = 4$) at 12 THz. The two modes are the perturbed dielectric slab mode [$\mathrm{Re}(k_\rho/k_0) \simeq 1$] and the graphene SP mode.

following we show that this is due to transfer of energy to a perturbed dielectric slab mode of the support structure; this also has severe consequences for modal confinement as shown below.

In order to identify the modes of the structure, Fig. 4 shows the radial plasmon wavenumber k_ρ (complex propagation constant) of the surface plasmon and related propagation modes of the structure as a function of slab thickness at 12 THz. Two modes are shown: one we refer to as the SP mode, which is the surface plasmon mode of the isolated graphene sheet slightly perturbed by the dielectric slab (this mode becomes the isolated graphene sheet SP as $d/\lambda \to 0$; the isolated/suspended graphene SP is also shown for reference), and the other is the TM surface wave of the dielectric slab slightly perturbed by the graphene sheet (i.e., the fundamental slab surface wave that propagates down to $d/\lambda \to 0$, and the only dielectric slab mode above cutoff at the considered frequencies), which we refer to as the dielectric-slab (DS) mode. The wavelength ratio of the suspended and supported graphene SP are $\lambda/\lambda_p = 17.4$ and 42.6, respectively, where the latter is insensitive to support thickness due to the tight confinement of the mode, and where $\lambda_p = 2\pi/\mathrm{Re}(k_\rho)$. This strong reduction in the plasmon wavelength has been experimentally verified; in Ref. 31 $\lambda/\lambda_p = 40$ was measured for graphene on SiC ($\varepsilon_r = 1.9$ at the experimental frequency), and good agreement was found with the formula

$$\frac{\lambda}{\lambda_p} = \frac{\hbar\omega(\varepsilon_r + 1)}{4\alpha\mu_c}, \qquad (1)$$

where $\alpha = 1/137$ is the fine-structure constant. For the parameters used to generate Fig. 4, Eq. (1) gives $\lambda/\lambda_p = 17.0$ and 42.5 for suspended and supported graphene, respectively, very close to the simulation values.

It is clear that the surface plasmon for supported graphene is slower and exhibits higher attenuation than for suspended graphene, associated with better field confinement to the lossy graphene surface compared to the suspended case. The faster dielectric slab mode has much lower attenuation, but extremely poor field confinement (since $d/\lambda \ll 1$; see Fig. 6). As discussed in Ref. 26 and references therein, the field along the interface and sufficiently far from the source will generally

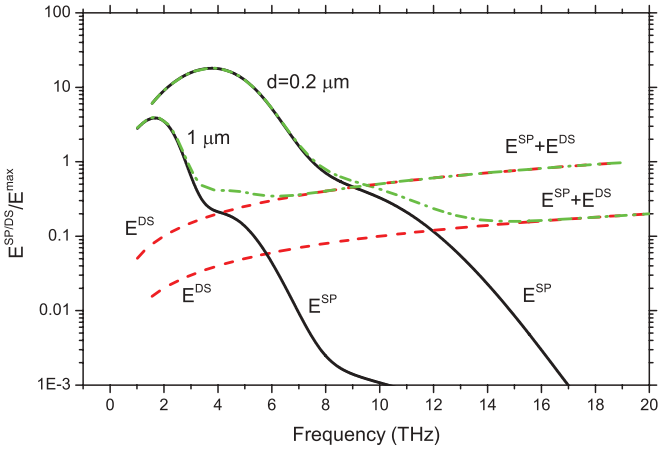

FIG. 5. (Color online) Residue part of the normalized vertical electric field for suspended graphene, associated with both SP propagation and the DS mode. Vertical position is $y = \lambda/100$, radial distance is $\rho/\lambda = 1$, $\mu_c = 0.2$ eV, and $\varepsilon_2 = 4$.

be dominated by discrete SP or surface-wave contributions, therefore in Fig. 5 we show the field due to the SP and surface wave contributions (residue part of the field[26]) for both SP and DS modes, for $d = 0.2$ μm and $d = 1$ μm. Both are obtained from pole singularities of the Sommerfeld integrals, Eq. (A5). In general, the two residues combine to form the total discrete modal field, $E^{\mathrm{SP}} + E^{\mathrm{DS}}$ (along with any other modes that are above cutoff). For $d = 1$ μm it is clear that the excitation peak near 2 THz is due to SP excitation, which diminishes rather

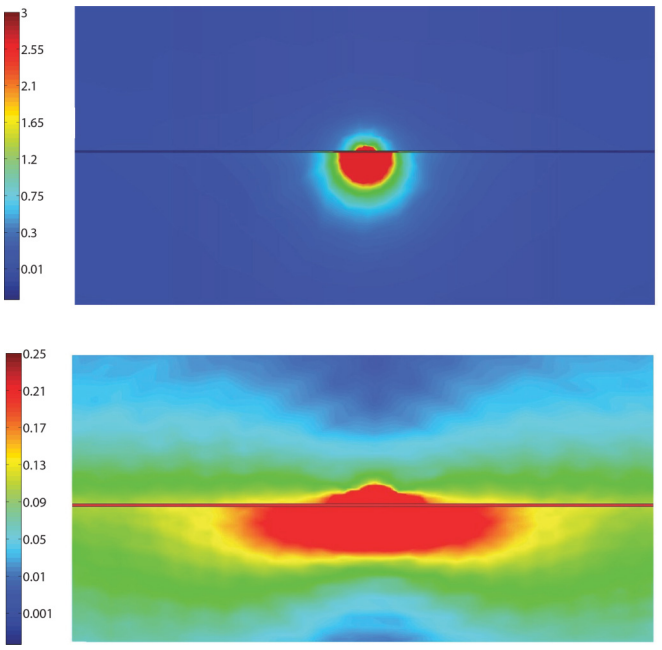

FIG. 6. (Color online) Scattered field profile in the cross section (2λ is shown) of supported graphene for $d = 1$ μm at 1 THz (top) and 12 THz (bottom), computed from the commercial finite-element software package HFSS. Results are shown in a plane perpendicular to the graphene sheet just in front ($x = \lambda/100$) of the vertical source dipole. The thin horizontal line is the dielectric slab (the graphene sheet is not visible at this scale), above and below which are the vacuum half-spaces.

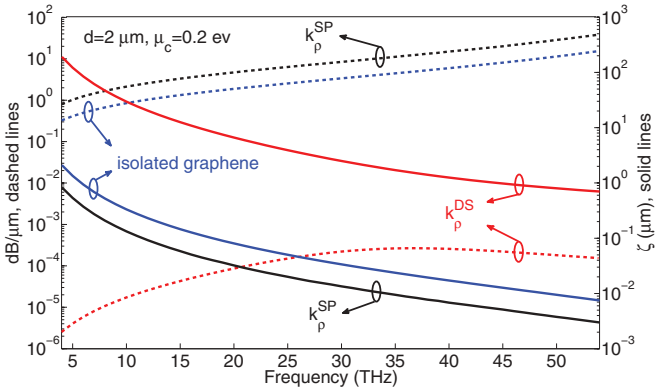

FIG. 7. (Color online) Power attenuation (dB/μm) and vertical confinement factor ζ for SP and DS modes, $\mu_c = 0.2$ eV.

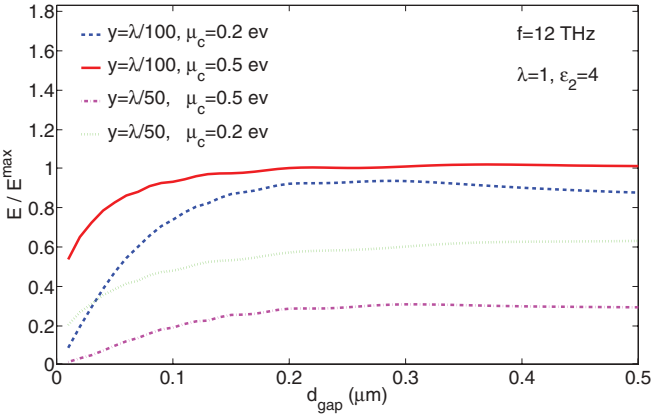

FIG. 8. (Color online) Normalized vertical field magnitude when the bottom layer has $\varepsilon_3 = 4$ and the slab material is vacuum, implementing an air gap between the graphene and lower half-space.

quickly with frequency, and above approximately 4 THz the field is mostly due to excitation of the dielectric slab mode with poor confinement. For $d = 0.2$ μm we see similar behavior, but shifted towards higher frequency (this blueshift as slab thickness decreases is consistent with Fig. 2).

Figure 6 shows the normalized scattered field profile in the cross section of the structure for $d = 1$ μm at two different frequencies, 1 and 12 THz, computed from the commercial finite-element software package HFSS.[40] The plot shows a 2λ area, and the graphene surface is modeled in HFSS using an impedance boundary condition.

At 1 THz the field is well confined, being associated with excitation of the graphene surface plasmon (consistent with the residue contribution in Fig. 5). Although not shown, at this frequency the decay rate of the field away from the graphene surface is similar for both suspended and supported graphene since the support only slightly perturbs the suspended graphene SP. However, at 12 THz the field is very poorly confined due to excitation of the dielectric slab mode rather than the SP mode (as evidenced by the residue contribution in Fig. 5), which is the cause of the extinction of the excitation peaks in Figs. 2 and 3. The spreading out of the energy in the vicinity of the source is considerable at 12 THz compared to at 1 THz, despite the vacuum wavelength being an order of magnitude smaller. In summary, Fig. 5 shows that the diminishment of the excitation peaks in Figs. 2 and 3, when a dielectric support is introduced, is due to transfer of energy to the perturbed DS mode of the support structure, with propagation characteristics shown in Fig. 4 (see also Fig. 7), and Fig. 6 confirms that the scattered field profile in space (including all possible contributions) is consistent with excitation of these two modes.

Figure 7 shows the power attenuation, $\alpha = 8.686\mathrm{Im}(k_\rho)$ for each mode, and also the normalized vertical confinement factor ζ (see Appendix). As described above, the SP mode on supported graphene has higher attenuation than on the suspended graphene sheet due to tighter field confinement, and the dielectric slab mode is very low-loss but very poorly confined as confirmed from the field plots (Fig. 6). Thus, due to excitation of the DS mode, supported graphene would seem to provide a poor platform for plasmonic applications compared to suspended graphene.

However, graphene rapidly (in space) decouples from the support structure. Figure 8 shows the normalized field when the bottom layer has $\varepsilon_3 = 4$ and the slab material is vacuum, implementing an air gap between the graphene and lower half-space. It can be seen that the graphene sheet effectively decouples from the substrate even for very small air gaps, with the results tending towards the corresponding isolated graphene result as d_{gap} increases. Not surprisingly, for sufficiently large air gaps (although still deep subwavelength, $d_{\mathrm{gap}}/\lambda = 0.008$ when $d_{\mathrm{gap}} = 0.2$ μm) the attractive plasmonic properties of suspended graphene are restored. The principle reasons for this rapid decoupling are the strong confinement of the SP mode, and the fact that the air gap forms an inverted waveguide such that energy cannot couple into a gap-supported mode (this is explained in more detail below).

It should be noted that this decoupling is electrodynamic, not electronic, although at the electronic level one would expect a similar decoupling (e.g., electron scattering on the graphene sheet would become independent of the lower half-space material). Note that we do not consider this type of electronic coupling even for the case of graphene on a substrate; we use a constant scattering rate γ throughout.

B. Graphene-SiO_2-Si geometry

Having examined the supported graphene case, we now consider the typical graphene-SiO_2-Si geometry. In Fig. 9 we show a result similar to that in Fig. 2, except when the bottom layer is Si (here we use a constant value of $\varepsilon_3 = 12$ and ignore losses; in this case λ is the wavelength in Si). For graphene directly on Si, the excitation peak is very low due to greatly increased field confinement near the lossy graphene. Note that, unlike the previous case of graphene on a dielectric slab, a (lossless) dielectric half-space cannot support a surface wave, and so if one regards the structure as an interacting system of isolated graphene and a dielectric half-space, there is no mode splitting as discussed above for supported graphene. In the present case, the large-permittivity half-space merely serves to concentrate the graphene fields, increasing attenuation which reduces the excitation peak.

When an SiO_2 layer is introduced between the graphene and Si the excitation peak is restored. This opposite behavior to the graphene-SiO_2-air case in Figs. 2 and 3 is easily explained: in the former the SiO_2 layer formed a weakly guiding dielectric

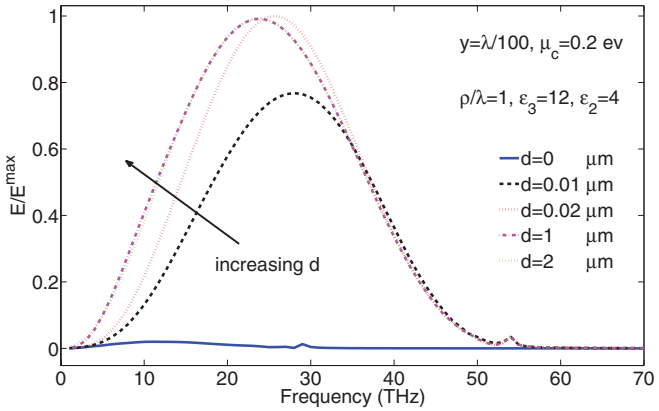

FIG. 9. (Color online) Normalized vertical electric field magnitude at vertical position $y = \lambda/100$ and radial distance $\rho/\lambda = 1$ (λ is wavelength in Si) for graphene on Si ($d = 0$, $\mu_c = 0.2$ eV) and for increasing slab thickness values for an $\varepsilon_2 = 4$ dielectric slab.

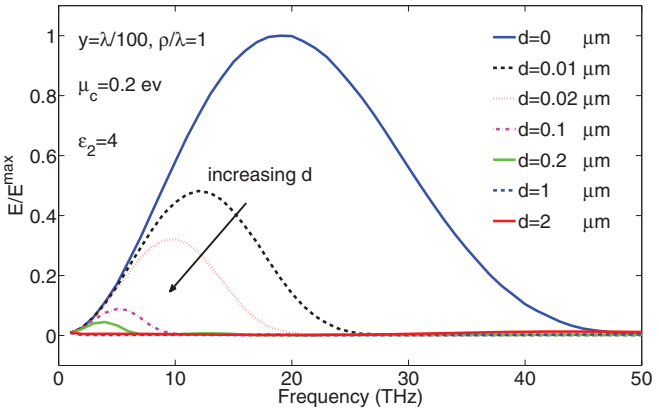

FIG. 11. (Color online) Normalized vertical electric field magnitude, Eq. (A7), at vertical position $y = \lambda/100$ and end-fire distance $\rho/\lambda = 1$ due to a horizontal dipole for a suspended graphene sheet ($d = 0$, $\mu_c = 0.2$ eV) and for supported graphene with increasing slab thickness values for an $\varepsilon_2 = 4$ dielectric slab.

waveguide, allowing for the transfer of energy into a perturbed DS mode as described previously. In the case of graphene-SiO_2-Si, we have something like an inverted waveguide (e.g., if we treat the graphene as sufficiently metal-like, then the dispersion equation of this structure would be the same as for Si-SiO_2-Si, the middle layer having double thickness) which cannot guide energy since $\varepsilon_{SiO_2} < \varepsilon_{Si}$.Therefore, the SiO_2 layer merely serves to form a spacer separating the graphene from the high-index Si, reducing field confinement somewhat and reducing attenuation, but still allowing a strong SP excitation peak. Only a perturbed SP mode exists (no DS mode can propagate) because of the inverted waveguide geometry. Thus, it can be concluded that the traditional graphene-SiO_2-Si system should have better SP properties than SiO_2 supported graphene. Potential absorption in the Si region should have minimal effect on the graphene SP due to tight field confinement, unless the Si is considerably lossy.

Figure 10 shows the modal attenuation and field confinement of the SP mode of the graphene-SiO_2-Si structure for various values of SiO_2 thickness. As expected, as thickness increases field confinement decreases and attenuation decreases.

Note that, compared to suspended graphene, the graphene-SiO_2-Si structure has stronger field confinementand, hence, increased attenuation, yet both geometries exhibit a strong excitation peak, as opposed to supported graphene. For example, for suspended graphene at 20 THz, $\alpha = 1.87$ dB/μm and $\zeta = 0.08$ μm. For a graphene-SiO_2-Si structure having $d_{SiO_2} = 200$ nm, $\alpha = 4.64$ dB/μm and $\zeta = 0.03$ μm, and so these structures have moderately similar characteristics at this frequency.

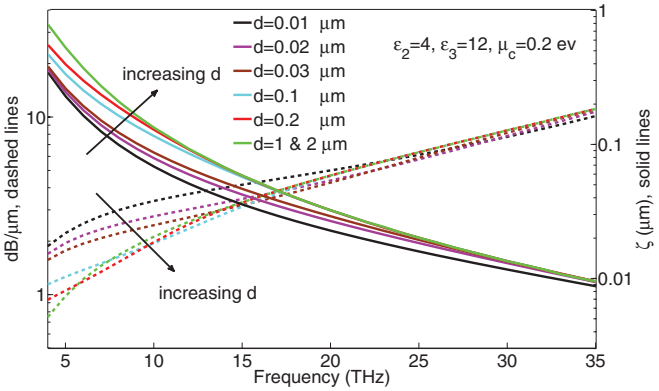

FIG. 10. (Color online) Modal attenuation and field confinement of the SP mode of the graphene-SiO_2-Si structure for various values of SiO_2 thickness.

C. Horizontal Dipole Source

The previous results have been obtained for vertical dipole excitation. In this section we briefly consider a horizontal dipole placed at the origin and oriented along the z axis, where the field generally has all three components $E_{x,y,z}$ and is given by Eqs. (A8)–(A10). On the graphene surface the broadside field ($z = 0$) has only a horizontal component E_z, Eq. (A8). Although for a dipole in free space this is the dominant field component, for a dipole on graphene this field is small, such that the normalized field $E_z/E_z^{\max}$ is of order 1 for all d values considered above (i.e., there is no strong excitation peak for the broadside field) and so we will omit results for this case. However, in the end-fire direction (along the z axis) both horizontal E_z and vertical E_y field components are large and exhibit a large excitation peak for suspended graphene. Figure 11 shows the vertical end-fire ($x = 0$, $\rho = z$) field for supported graphene. As substrate thickness increases the excitation peak is diminished, similar to Figs. 2 and 3; this behavior is explained by the same phenomena as described above. On the graphene surface the horizontal endfire field is essentially identical to the vertical field shown in Fig. 11, and so is omitted here. Note that the fields in Fig. 11 are normalized by the broadside field λ away from the dipole, since in the absence of the graphene and dielectric layers the end-fire field is very small.

D. Spontaneous decay rate

For a two-level quantum emitter modeled as a vertical dipole source $\mathbf{J} = j\omega\mathbf{p}\delta(\mathbf{r} - \mathbf{r}_0)$, where $\mathbf{p} = p\mathbf{n}_p$ is the dipole moment of magnitude p, then the spontaneous decay rate

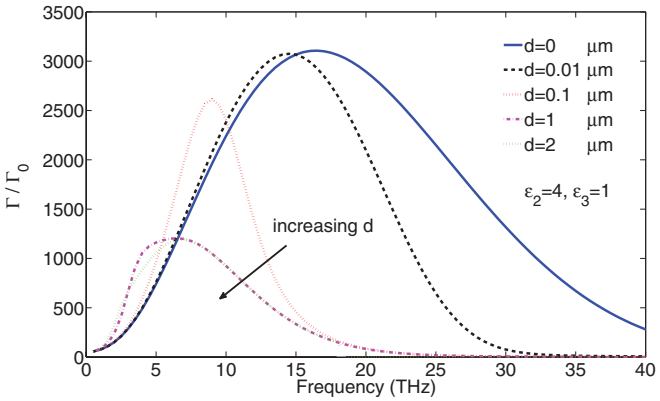

FIG. 12. (Color online) Purcell factor for supported graphene ($\varepsilon_2 = 4$, $\varepsilon_1 = \varepsilon_3 = 1$) as a function of frequency for dipole position $y = \lambda/100$ and $\mu_c = 0.2$ eV.

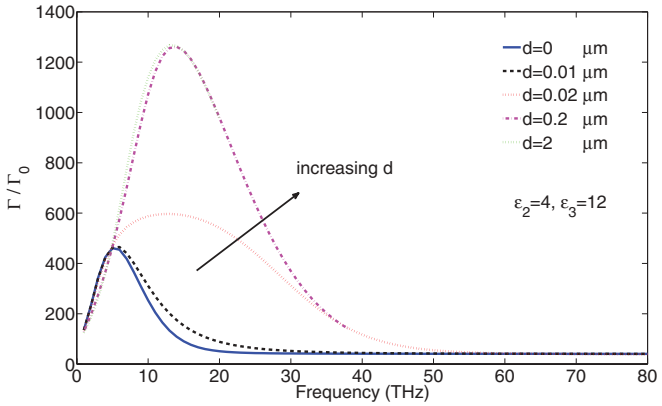

FIG. 13. (Color online) Purcell factor for graphene-SiO_2-Si ($\varepsilon_2 = 4$, $\varepsilon_1 = 1$, $\varepsilon_3 = 12$) as a function of frequency for dipole position $y = \lambda/100$ and $\mu_c = 0.2$ eV.

(SDR) is[41]

$$\Gamma = \frac{2\omega}{3\hbar\varepsilon_0}|\mathbf{p}|^2\left[\frac{6\omega}{\pi c^2}\mathrm{Im}\{\mathbf{n}_p\cdot\mathbf{G}(\mathbf{r}_0,\mathbf{r}_0)\cdot\mathbf{n}_p\}\right], \tag{2}$$

where the bracketed quantity is the partial local density of photonic states (LDOS). The Green's dyadic in the notation of Ref. 41 is defined such that $\mathbf{E} = \omega^2\mu_0\mathbf{G}\cdot\mathbf{p}$; using the notation for the Green's functions in this work, $\mathbf{G}$ in (2) must be replaced by $\mathbf{G}\varepsilon_0/k_0^2$ assuming the top layer is vacuum. In Ref. 28 the Purcell factor was also examined for graphene in the presence of one and two emitters, without the dielectric support slab. Here we focus on the vertical dipole excitation, since the end-fire fields of the horizontal dipole behave similarly.

The total decay rate (free space plus that due to the dielectric slab) is

$$\begin{aligned}\Gamma &= \Gamma_0 + \Gamma_R \\ &= \frac{|\mathbf{p}|^2}{2\pi\hbar\varepsilon_0}\mathrm{Im}\left(\int_0^\infty \frac{q^3}{\sqrt{q^2-k_0^2}}(1+R_n e^{-2\sqrt{q^2-k_0^2}x})dq\right),\end{aligned} \tag{3}$$

where we used $\rho = 0$, $J_0(0) = 1$. In free space ($R_n = 0$) it is easy to evaluate the first term in (3) to obtain the well known result $\Gamma_0 = k_0^3|\mathbf{p}|^2/3\pi\hbar\varepsilon_0$, and so the normalized SDR (Purcell factor) is

$$\begin{aligned}\frac{\Gamma}{\Gamma_0} &= 1 + \frac{\Gamma_s}{\Gamma_0} \\ &= 1 - \frac{1}{k_2^3}\frac{3}{2}\mathrm{Im}\left(\int_0^\infty \frac{q^3}{\sqrt{q^2-k_2^2}}R_n e^{-2\sqrt{q^2-k_2^2}x}dq\right).\end{aligned} \tag{4}$$

Figure 12 shows the Purcell factor as a function of frequency for dipole position $y = \lambda/100$. It can be seen that the presence of the graphene results in a very large decay rate, reflecting the large photonic density of states associated with additional decay channels due to the graphene SP modes. However, the presence of the dielectric slab shifts the peak and reduces the decay rate, saturating for larger slab thickness. This behavior is similar to the classical forced dipole excitation shown in Figs. 2 and 3 with a similar explanation.

In Fig. 13 we show the Purcell factor for graphene-SiO_2-Si. It can be seen that the addition of an $\varepsilon_2 = 4$ layer between the graphene and the Si enhances the SDR, which is the opposite effect observed in Fig. 12. This is consistent with the result for the classical dipole, where Fig. 10 shows behavior opposite to that of Fig. 2; the explanation is the same as in the previous case. This correspondence between classical dipole excitation and the LDOS is expected, and in Ref. 31 it was shown that the calculated LDOS for a tapered graphene ribbon agreed very well with the SNOM data.

IV. CONCLUSIONS

The excitation of TM surface plasmons by vertical and horizontal dipoles on graphene has been examined. It has been shown that for suspended graphene (i.e., in the presence of a finite-thickness dielectric support layer such as SiO_2) considerable spectral content is transferred to a perturbed dielectric slab mode, greatly decreasing and redshifting the excitation peak and resulting in very poor field confinement of the mode. For graphene on a Si half-space the excitation strength is also diminished but without lessening field confinement (in fact, field confinement is increased). For graphene on top of SiO_2-Si, the presence of the SiO_2 layer creates a spacer restoring the excitation peak. A two-level quantum emitter was also considered, and it was shown that the addition of a thin dielectric support slab and SiO_2-Si geometries affects the spontaneous decay rate in a manner similar to the classical dipole SP excitation peak.

APPENDIX

For the conductivity of graphene we use the expression resulting from the Kubo formula,[36]

$$\begin{aligned}&\sigma(\omega,\mu_c,\gamma,T) \\ &= -j\frac{e^2k_BT}{\pi\hbar^2(\omega-j\gamma)}\left(\frac{\mu_c}{k_BT}+2\ln(e^{-\frac{\mu_c}{k_BT}}+1)\right) \\ &\quad -\frac{je^2(\omega-j\gamma)}{\pi\hbar^2}\int_0^\infty\frac{f_d(-\varepsilon)-f_d(\varepsilon)}{(\omega-j\gamma)^2-4(\varepsilon/\hbar)^2}d\varepsilon,\end{aligned} \tag{A1}$$

where e is the charge of an electron, $\hbar = h/2\pi$ is the reduced Planck's constant, $f_d(\varepsilon) = (e^{(\varepsilon-\mu_c)/k_BT}+1)^{-1}$ is the Fermi-Dirac distribution, and k_B is Boltzmann's constant. The first term in (A1) is due to intraband contributions, and the second term to interband contributions.

The Green's functions for the structure depicted in Fig. 1 are similar to those used in Ref. 26 (see also Refs. 11 and 42), with a modification of the coefficients to account for the different graphene/dielectric regions. The electric and magnetic fields in region α due to a source in region β of the geometry depicted in Fig. 1 are

$$\begin{aligned}\mathbf{E}^{(\alpha,\beta)}(\mathbf{r}) &= \left(k_\alpha^2 + \nabla\nabla\cdot\right)\boldsymbol{\pi}^{(\alpha,\beta)}(\mathbf{r}),\\ \mathbf{H}^{(\alpha,\beta)}(\mathbf{r}) &= j\omega\varepsilon_\alpha\nabla\times\boldsymbol{\pi}^{(\alpha,\beta)}(\mathbf{r}),\end{aligned} \tag{A2}$$

where $k_\alpha = \omega\sqrt{\mu_\alpha\varepsilon_\alpha}$ and $\boldsymbol{\pi}(\mathbf{r})$ are the wavenumber and electric Hertzian potential, respectively. The Hertzian potential is

$$\begin{aligned}\boldsymbol{\pi}^{(\alpha,\beta)}(\mathbf{r}) &= \boldsymbol{\pi}^{\mathrm{p}}_{\alpha,\beta}(\mathbf{r})\delta_{\alpha,\beta} + \boldsymbol{\pi}^{\mathrm{s}}_{\alpha,\beta}(\mathbf{r})\\ &= \int_\Omega \left\{\underline{\mathbf{g}}^{\mathrm{p}}_\beta(\mathbf{r},\mathbf{r}')\delta_{\alpha,\beta} + \underline{\mathbf{g}}^{\mathrm{s}}_{\alpha,\beta}(\mathbf{r},\mathbf{r}')\right\}\cdot\frac{\mathbf{J}^{(\beta)}(\mathbf{r}')}{j\omega\varepsilon_\beta}\,d\Omega',\end{aligned} \tag{A3}$$

where the underscore indicates a dyadic quantity, $\delta_{\alpha,\beta}$ is the Kronecker delta function, and Ω is the support of the current, and where

$$\begin{aligned}\underline{\mathbf{g}}^{\mathrm{p}}_\beta(\mathbf{r},\mathbf{r}') &= \underline{\mathbf{I}}\,\frac{e^{-jk_\beta R}}{4\pi R} = \underline{\mathbf{I}}\,g^h_\beta(\mathbf{r},\mathbf{r}')\\ &= \underline{\mathbf{I}}\,\frac{1}{2\pi}\int_{-\infty}^{\infty} e^{-p_\beta|y-y'|}\frac{H_0^{(2)}(k_\rho\rho)}{4p_\beta}k_\rho dk_\rho,\\ \underline{\mathbf{g}}^{\mathrm{s}}_{\alpha,\beta}(\mathbf{r},\mathbf{r}') &= \widehat{\mathbf{y}}\widehat{\mathbf{y}}g^{\mathrm{n}}_{\alpha,\beta}(\mathbf{r},\mathbf{r}') + \left(\widehat{\mathbf{y}}\widehat{\mathbf{x}}\frac{\partial}{\partial x} + \widehat{\mathbf{y}}\widehat{\mathbf{z}}\frac{\partial}{\partial z}\right)g^{\mathrm{c}}_{\alpha,\beta}(\mathbf{r},\mathbf{r}')\\ &\quad + (\widehat{\mathbf{x}}\widehat{\mathbf{x}} + \widehat{\mathbf{z}}\widehat{\mathbf{z}})g^{\mathrm{t}}_{\alpha,\beta}(\mathbf{r},\mathbf{r}'),\end{aligned} \tag{A4}$$

$\underline{\mathbf{I}}$ is the unit dyadic, k_ρ is a radial wavenumber, $p_\alpha^2 = k_\rho^2 - k_\alpha^2$, $\rho = \sqrt{(x-x')^2+(z-z')^2}$, and $R = |\mathbf{r}-\mathbf{r}'| = \sqrt{(y-y')^2+\rho^2}$. The Green's function components are given as Sommerfeld integrals,

$$\begin{aligned}g^{\nu}_{\alpha,\beta}(\mathbf{r},\mathbf{r}') &= \frac{1}{2\pi}\int_{-\infty}^{\infty} R^{\nu}_{\alpha,\beta}(k_\rho,y,y')\frac{H_0^{(2)}(k_\rho\rho)}{4p_\beta}k_\rho dk_\rho\\ &= \frac{1}{2\pi}\int_0^{\infty} R^{\nu}_{\alpha,\beta}(k_\rho,y,y')\frac{J_0(k_\rho\rho)}{2p_\beta}k_\rho dk_\rho,\end{aligned} \tag{A5}$$

$\nu = t,n,c$, with coefficients $R^{\nu}_{1,1}$ provided in this Appendix. Surface plasmons supported by the structure result from the zeros of the dominators of $R^{\nu}_{\alpha,\beta}$,

$$Z^{\mathrm{TM/TE}}(k_\rho,\omega) = 0, \tag{A6}$$

where TM/TE indicates transverse magnetic/electric fields with respect to the mode propagation direction.

The wave parameters $p_\alpha = \sqrt{k_\rho^2 - k_\alpha^2}$, $\alpha = 1,3$, lead to nonremovable branch points at $k_\rho = \pm k_\alpha$ (the branch points associated with p_2, and, more generally with any "middle layers" that do not extend to vertical infinity, are removable[43]) and thus the k_ρ plane is a four-sheeted Riemann surface. The standard hyperbolic branch cuts[43,44] that separate the one proper sheet [where $\mathrm{Re}(p_{1,3}) > 0$, such that the radiation condition as $|y| \to \infty$ is satisfied] and the three improper sheets are the same as in Ref. 26.

Here we consider a vertical and horizontal point source $\mathbf{J} = A_0\widehat{\mathbf{c}}\delta(\mathbf{r}-\mathbf{r}_0), \widehat{\mathbf{c}} = \widehat{\mathbf{y}},\widehat{\mathbf{z}}$, where $\mathbf{r}_0 \simeq \mathbf{0}$ is just above the graphene sheet ($y = \lambda/100$) in region 1. For convenience we set $A_0 = 1$ A. Both vertical and horizontal dipoles excite all three field components $E_{x,y,z}$. As discussed above we concentrate on the ϕ-symmetric vertical electric field

$$\begin{aligned}E_y^{(1,1)}(\mathbf{r}) &= E^{\mathrm{h}} + E^{\mathrm{s}}\\ &= \frac{1}{j\omega\varepsilon_1}\left(k_1^2 + \frac{\partial^2}{\partial y^2}\right)\left[g_1^{\mathrm{h}}(\mathbf{r}) + g_{1,1}^{\mathrm{n}}(\mathbf{r})\right],\end{aligned} \tag{A7}$$

where the first term is the vertical component of the direct source-excited field in free space (in the absence of the graphene/dielectric layers), $R = \sqrt{x^2+y^2+z^2}$, and the second term is the response of the layered medium. As discussed in Ref. 26 the layered medium response can be decomposed into discrete surface plasmons (residues) and the radiation field (branch cut integral) components via complex-plane analysis, although in most of the following we compute the field as an integral along the real axis.

A horizontal dipole ($\widehat{\mathbf{c}} = \widehat{\mathbf{z}}$) excites both TM and TE modes, but for the thin dielectric layers considered here TE modes are below cutoff and TM modes are of predominate interest. The field components are

$$\begin{aligned}E_x^{(1,1)} &= \frac{1}{j\omega\varepsilon_1}\left(\frac{\partial^2}{\partial x\,\partial z}\left[g_1^{\mathrm{h}}(\mathbf{r}) + g_{1,1}^{\mathrm{t}}(\mathbf{r})\right] + \frac{\partial^3}{\partial x\,\partial y\,\partial z}g_{1,1}^{\mathrm{c}}(\mathbf{r})\right),\\ E_y^{(1,1)} &= \frac{1}{j\omega\varepsilon_1}\left[\frac{\partial^2}{\partial y\,\partial z}g_1^{\mathrm{h}}(\mathbf{r}) + \left(k^2 + \frac{\partial^2}{\partial y^2}\right)\frac{\partial}{\partial z}g_{1,1}^{\mathrm{c}}(\mathbf{r}) + \frac{\partial^2}{\partial y\partial z}g_{1,1}^{\mathrm{t}}(\mathbf{r})\right],\\ E_z^{(1,1)} &= \frac{1}{j\omega\varepsilon_1}\left[\left(k_1^2 + \frac{\partial^2}{\partial z^2}\right)\left[g_1^{\mathrm{h}}(\mathbf{r}) + g_{1,1}^{\mathrm{t}}(\mathbf{r})\right] + \frac{\partial^3}{\partial z^2\partial y}g_{1,1}^{\mathrm{c}}(\mathbf{r})\right].\end{aligned} \tag{A8}$$

For the special case of the field broadside to the dipole ($z = 0$), on the graphene surface the fields are ($\rho = x$)

$$\begin{aligned}E_x^{(1,1)} &= E_y^{(1,1)} = 0,\\ E_z^{(1,1)} &= \left(k^2 + \frac{\partial^2}{\partial z^2}\right)g_1^{\mathrm{h}}(\mathbf{r}) + \frac{1}{2\pi}\int_0^{\infty}\frac{-qe^{-p_1 y}}{2p_1 j\omega\varepsilon_1}\left\{-k_1^2R_{1,1}^{\mathrm{t}}J_0(q\rho) + q\left[R_{1,1}^{\mathrm{t}} - p_1R_{1,1}^{\mathrm{c}}\right]\frac{1}{\rho}J_1(q\rho)\right\}dq.\end{aligned} \tag{A9}$$

For the special case of the field end-fire to the dipole ($x = 0$), on the graphene surface the fields are

$$E_x^{(1,1)} = 0,$$
$$E_y^{(1,1)} = \frac{1}{j\omega\varepsilon_1}\frac{\partial^2}{\partial y\partial z}g_1^{\mathrm{h}}(\mathbf{r}) + \frac{1}{2\pi}\int_0^\infty \left[\left(k_1^2 + p_1^2\right)R_{1,1}^{\mathrm{c}} - p_1 R_{1,1}^{\mathrm{t}}\right]\frac{-q^2 e^{-p_1 y}}{2p_1 j\omega\varepsilon_1}J_1(q\rho)\,dq,$$
$$E_z^{(1,1)} = \frac{1}{j\omega\varepsilon_1}\left(k_1^2 + \frac{\partial^2}{\partial z^2}\right)g_1^{\mathrm{h}}(\mathbf{r}) + \frac{1}{2\pi}\int_0^\infty \frac{-qe^{-p_1 y}}{2p_1 j\omega\varepsilon_1}\left\{q^2\left[R_{1,1}^{\mathrm{t}} - p_1 R_{1,1}^{\mathrm{c}}\right]\left[J_0(q\rho) + \frac{1}{q\rho}J_1(q\rho)\right] - k_1^2 R_{1,1}^{\mathrm{t}} J_0(q\rho)\right\}dq. \tag{A10}$$

In the numerical results all fields are normalized by the field of a dipole in free space evaluated at λ broadside from the dipole,

$$|E^h| = E^{\max} = \frac{1}{2\pi c\varepsilon_1\lambda^2}\frac{\sqrt{16\pi^4 - 4\pi^2 + 1}}{4\pi} \simeq \frac{3.1}{2\pi c\varepsilon_1\lambda^2}, \tag{A11}$$

which is the largest field produced by the dipole (when in free space), where c is the vacuum velocity of light.

The degree of confinement of the surface plasmon to the graphene layer can be gauged by defining a vertical attenuation length ζ, at which point the wave decays to $1/e$ of its value on the surface. Given the vertical dependence of the reflection coefficients $R_{1,1}^{t,n,c}$, $\zeta^{-1} = \mathrm{Re}(p_1) = \mathrm{Re}(\sqrt{(k_\rho^{\mathrm{SP}})^2 - k_1^2})$.

The Sommerfeld integral coefficients for the geometry depicted in Fig. 1 are (here the permittivities are total, not relative values, and so include the free-space permittivity ε_0)

$$R_{1,1}^{\mathrm{t}} = \frac{A_1^{\mathrm{t}}\cosh(p_2 d) + A_2^{\mathrm{t}}\sinh(p_2 d)}{Z_1^{\mathrm{t}}\cosh(p_2 d) + Z_2^{\mathrm{t}}\sinh(p_2 d)}e^{-p_1(y+y')} = \frac{N^{\mathrm{TE}}(k_\rho,\omega)}{Z^{\mathrm{TE}}(k_\rho,\omega)}e^{-p_1(y+y')}, \tag{A12}$$

$$R_{1,1}^{\mathrm{n}} = \frac{A_1^{\mathrm{n}}\cosh(p_2 d) + A_2^{\mathrm{n}}\sinh(p_2 d)}{Z_1^{\mathrm{n}}\cosh(p_2 d) + Z_2^{\mathrm{n}}\sinh(p_2 d)}e^{-p_1(y+y')} = \frac{N^{\mathrm{TM}}(k_\rho,\omega)}{Z^{\mathrm{TM}}(k_\rho,\omega)}e^{-p_1(y+y')}, \tag{A13}$$

$$R_{1,1}^{\mathrm{c}} = \frac{p_1}{p_2\omega}\frac{B + C\cosh(2dp_2) + D\sinh(2dp_2)}{Z^{\mathrm{TE}}(k_\rho,\omega)Z^{\mathrm{TM}}(k_\rho,\omega)}e^{-p_1(y+y')}, \tag{A14}$$

$$A_1^{\mathrm{t}} = p_2(p_1 - p_3 - j\omega\mu_0\sigma), \quad A_2^{t} = p_1 p_3 - p_2^2 - j\omega\mu_0\sigma p_3, \tag{A15}$$

$$Z_1^{\mathrm{t}} = p_2(p_1 + p_3 + j\omega\mu_0\sigma), \quad Z_2^{t} = p_1 p_3 + p_2^2 + j\omega\mu_0\sigma p_3, \tag{A16}$$

$$A_1^{\mathrm{n}} = \varepsilon_2\left[\frac{p_1 p_3}{j\omega}\sigma + p_1\varepsilon_3 - \varepsilon_1 p_3\right], \tag{A17}$$

$$A_2^{\mathrm{n}} = p_2\left[\frac{p_1 p_3}{p_2^2}\varepsilon_2^2 - \varepsilon_1\varepsilon_3 + \frac{p_1\varepsilon_3\sigma}{j\omega}\right], \tag{A18}$$

$$Z_1^{\mathrm{n}} = \varepsilon_2\left[\frac{p_1 p_3}{j\omega}\sigma + p_1\varepsilon_3 + \varepsilon_1 p_3\right], \tag{A19}$$

$$Z_1^{\mathrm{n}} = \varepsilon_2\left[\frac{p_1 p_3}{j\omega}\sigma + p_1\varepsilon_3 + \varepsilon_1 p_3\right], \tag{A20}$$

$$Z_1^{\mathrm{n}} = \varepsilon_2\left[\frac{p_1 p_3}{j\omega}\sigma + p_1\varepsilon_3 + \varepsilon_1 p_3\right], \tag{A21}$$

$$Z_2^{\mathrm{n}} = p_2\left[\frac{p_1 p_3}{p_2^2}\varepsilon_2^2 + \varepsilon_1\varepsilon_3 + \frac{p_1\varepsilon_3\sigma}{j\omega}\right], \tag{A22}$$

$$B = p_3^2\varepsilon_2\omega(\varepsilon_1 - \varepsilon_2) - jp_2^2 p_3\sigma(\varepsilon_2 - \varepsilon_3) + p_2^2\omega(\varepsilon_3(\varepsilon_1 + \varepsilon_2) - 2\varepsilon_1\varepsilon_2), \tag{A23}$$

$$C = -jp_2^2 p_3\sigma(\varepsilon_2 + \varepsilon_3) + \omega p_3^2(\varepsilon_2 - \varepsilon_1)(\varepsilon_2 + \varepsilon_3), \tag{A24}$$

$$D = -jp_2\sigma\left(p_3^2\varepsilon_2 + p_2^2\varepsilon_3\right) + \omega p_2 p_3(\varepsilon_2 - \varepsilon_1)(\varepsilon_2 + \varepsilon_3). \tag{A25}$$

*george@uwm.edu
†eforati@uwm.edu
‡wwlinz@uwm.edu
§yakovlev@olemiss.edu

[1] A. Reina, X. Jia, J. Ho, D. Nezich, H. Son, V. Bulovic, M. S. Dresselhaus, and J. Kong, Nano Lett. **9**, 30 (2009).
[2] X. Li, W. Cai, J. An, S. Kim, J. Nah, D. Yang, R. Piner, A. Velamakanni, I. Jung, E. Tutuc, S. K. Banerjee, L. Colombo, and R. S. Ruoff, Science **324**, 1312 (2009).
[3] F. Rana, IEEE Trans. Nano Technol. **7**, 91 (2008).
[4] Q. Bao, H. Zhang, B. Wang, Z. Ni, C. H. Y. X. Lim, Y. Wang, D. Y. Tang, and K. P. Loh, Nature Photonics **5**, 411 (2011).
[5] J. T. Kim and C.-G. Choi, Opt. Express **20**, 3556 (2012).
[6] H. Yan, X. Li, B. Chandra, G. Tulevski, Y. Wu, M. Freitag, W. Zhu, P. Avouris, and F. Xia, Nature Nanotechnol. **7**, 330 (2012).
[7] P. Liu, W. Cai, L. Wang, X. Zhang, and J. Xu, Appl. Phys. Lett. **100**, 153111 (2012).
[8] I. Llatsera, C. Kremers, A. Cabellos-Aparicio, J. M. Jornet, E. Alarcón, and D. N. Chigrin, Photonics Nanostruct. **10**, 353 (2012).
[9] D. R. Anderson, J. Opt. Soc. Am. B **27**, 818 (2010).

[10] A. Vakil and N. Engheta, Science **332**, 1291 (2011).
[11] G. W. Hanson, J. Appl. Phys. **104**, 084314 (2008).
[12] C. Xu, H. Li, and K. Banerjee, IEEE Trans. Electron Devices **56**, 1567 (2009).
[13] G. Deligeorgis, M. Dragoman, D. Neculoiu, D. Dragoman, G. Konstantinidis, A. Cismaru, and R. Plana, Appl. Phys. Lett. **95**, 073107 (2009).
[14] V. V. Popov, T. Y. Bagaeva, T. Otsuji, and V. Ryzhii, Phys. Rev. B **81**, 073404 (2010).
[15] M. Dragoman, D. Neculoiu, A. Cismaru, A. A. Muller, G. Deligeorgis, G. Konstantinidis, D. Dragoman, and R. Plana, Appl. Phys. Lett. **99**, 033112 (2011).
[16] B. Wang, X. Zhang, X. Yuan, and J. Teng, Appl. Phys. Lett. **100**, 131111 (2012).
[17] S. Thongrattanasiri, A. Manjavacas, and F. J. G. de Abajo, ACS Nano **6**, 1766 (2012).
[18] A. Vakil and N. Engheta, Phys. Rev. B **85**, 075434 (2012).
[19] H. J. Xu, W. B. Lu, Y. Jiang, and Z. G. Dong, Appl. Phys. Lett. **100**, 051903 (2012).
[20] P.-Y. Chen and A. Alù, ACS Nano **5**, 5855 (2011).
[21] O. Vafek, Phys. Rev. Lett. **97**, 266406 (2006).
[22] A. Bostwick, T. Ohta, T. Seyller, K. Horn, and E. Rotenberg, Nat. Phys. **3**, 36 (2007).
[23] B. Wunsch, T. Stauber, F. Sols, and F. Guinea, New J. Phys. **8**, 318 (2006).
[24] E. H. Hwang and S. Das Sarma, Phys. Rev. B **75**, 205418 (2007).
[25] S. A. Mikhailov and K. Ziegler, Phys. Rev. Lett. **99**, 016803 (2007).
[26] G. W. Hanson, A. B. Yakovlev, and A. Mafi, J. Appl. Phys. **110**, 114305 (2011).
[27] A. Y. Nikitin, F. Guinea, F. J. Garcia-Vidal, and L. Martin-Moreno, Phys. Rev. B **84**, 195446 (2011).
[28] P. A. Huidobro, A. Y. Nikitin, C. González-Ballestero, L. Martín-Moreno, and F. J. García-Vidal, Phys. Rev. B. **85**, 155438 (2012).
[29] L. Ju, B. Geng, J. Horng, C. Girit, M. Martin, Z. Hao, H. A. Bechtel, X. Liang, A. Zettl, Y. R. Shen, and F. Wang, Nature Nanotechnol. **6**, 630 (2011).
[30] Z. Fei, G. O. Andreev, W. Bao, L. M. Zhang, A. S. McLeod, C. Wang, M. K. Stewart, Z. Zhao, G. Dominguez, M. Thiemens, M. M. Fogler, M. J. Tauber, A. H. Castro-Neto, C. N. Lau, F. Keilmann, and D. N. Basov, Nano Lett. **11**, 4701 (2011).
[31] J. Chen, M. Badioli, P. Alonso-González, S. Thongrattanasiri, F. Huth, J. Osmond, M. Spasenović, A. Centeno, A. Pesquera, P. Godignon, A. Z. Elorza, N. Camara, F. J. G. de Abajo, R. Hillenbrand, and F. H. L. Koppens, Nature (London) **487**, 77 (2012).
[32] J. C. Meyer, A. K. Geim, M. I. Katsnelson, K. S. Novoselov, T. J. Booth, and S. Roth, Nature (London) **446**, 60 (2007).
[33] R. R. Nair, P. Blake, A. N. Grigorenko, K. S. Novoselov, T. J. Booth, T. Stauber, N. M. R. Peres, and A. K. Geim, Science **320**, 1308 (2008).
[34] J. Hun Seol, I. Jo, A. L. Moore, L. Lindsay, Z. H. Aitken, M. T. Pettes, X. Li, Z. Yao, R. Huang, D. Broido, N. Mingo, R. S. Ruoff, and L. Shi, Science **328**, 213 (2010).
[35] A. Reina, X. Jia, J. Ho, D. Nezich, H. Son, V. Bulovic, M. S. Dresselhaus, and J. Kong, Nano Lett. **9**, 30 (2009).
[36] V. P. Gusynin, S. G. Sharapov, and J. P. Carbotte, J. Phys.: Condens. Matter **19**, 026222 (2007).
[37] Z. Q. Li, E. A. Henriksen, Z. Jiang, Z. Hao, M. C. Martin, P. Kim, H. L. Stormer, and D. N. Basov, Nature Phys. **4**, 532 (2008).
[38] C. Lee, J. Y. Kim, S. Bae, K. S. Kim, B. H. Hong, and E. J. Choi, Appl. Phys. Lett. **98**, 071905 (2011).
[39] J. Y. Kim, C. Lee, S. Bae, K. S. Kim, B. H. Hong, and E. J. Choi, Appl. Phys. Lett. **98**, 201907 (2011).
[40] High Frequency Structure Simulator (HFSS) version 12.0, Ansys Corporation, PA, 2012, http://www.ansys.com
[41] L. Novotny and B. Hecht, *Principles of Nano-Optics* (Cambridge University Press, Cambridge, UK, 2006).
[42] G. W. Hanson, IEEE Trans. Antennas Propagat. **56**, 747 (2008).
[43] W. C. Chew, *Waves and Fields in Inhomogeneous Media* (IEEE, Piscataway, NJ, 1991).
[44] A. Ishimaru, *Electromagnetic Wave Propagation, Radiation, and Scattering* (Prentice Hall, Englewood Cliffs, NJ, 1991).